Published 03/28/2017

doi:10.4271/2017-01-1218
saealtpow.saejournals.org

Development and Validation of a Reduced Order Model Incorporating a Semi-Empirical Degradation Model for Pouch Type $LiFePO_4$/Graphite Cells

XINCHEN ZHAO, Yalan Bi, and Song-Yul Choe
Auburn University

ABSTRACT

We propose a reduced order model (ROM) for LFP/graphite cells derived from the electrochemical thermal principles that considers degradation effects and validated against experimental data obtained from a large format pouch type LFP/graphite cell whose nominal capacity is 20Ah. The characteristics of the two-phase transition and path dependence were taken into account in the ROM using a shrinking-core model with a moving interface that presents lithium rich and deficient phase. Different currents (0.1/1/3/4C) were applied to fresh cells at different ambient temperatures (25/35/45°C). Comparison between simulated results of the ROM and the collected experimental data shows a good match. The path dependence was also analyzed experimentally. For degradation model, side reaction is treated as the predominant cause of degradation of cells, which are affected by the operating conditions, such as temperature and SOC cycling range. At every 30 or 40 cycles, the capacity and impedance of five cycled cells were measured under different temperatures and SOC cycling ranges. The final capacity fades were 5.81%, 10.95%, 12.17%, 14.17%, and 23.54%, respectively. Degradation was accelerated by elevated temperature and high SOC cycling range. A semi-empirical degradation model was incorporated into the developed ROM. Three key parameters, the volume fraction of active anode material, the resistance of SEI and deposit layer, and the effective diffusion coefficient in the electrolyte, were extracted from experiments using the nonlinear least square method. The simulation results and experimental data are in a pretty good match.

CITATION: ZHAO, X., Bi, Y., and Choe, S., "Development and Validation of a Reduced Order Model Incorporating a Semi-Empirical Degradation Model for Pouch Type LiFePO4/Graphite Cells," *SAE Int. J. Alt. Power.* 6(2):2017, doi:10.4271/2017-01-1218.

INTRODUCTION

Lithium iron phosphate (LFP), a promising cathode material with characteristics of good electrochemical and thermal stability, was firstly introduced by Padhi [1] et al. in 1997. It has attracted much attention from researchers and its applications in both small portable devices, such as laptops, and mobile phones, and high power electric and hybrid electric vehicles have been investigated [2, 3, 4].

The behaviors of the battery given by the ion transport, intercalation, and deintercalation as well as states are approximated with two methods, equivalent circuit model (ECM) and the physics-based electrochemical thermal model. Even though the ECMs have the strengths of fast calculating and accuracy, ECMs are still limited by its great dependence on experiments and empirical parameters. [5] Electrochemical thermal models based on physical principles compensate the weaknesses of ECMs with the predictive capability of electrodes dynamics. However, the calculation speed is relatively slower than that of the ECMs.

For lithium-ion batteries, the sandwich model was firstly proposed by Doyle [6], which simulated the galvanostatic discharge/charge behaviors with the concentrated solution theory, including electrodes kinetics and ion transport. A typical electrochemical model usually contained the intercalation/deintercalation of lithium ions to/from the electrodes, chemical reactions at the interface between electrode and electrolyte, and diffusion of lithium ions through solid particles and electrolyte. For electrodes embedded by Ni, Mn, Co, only single phase exists during charge and discharge. For certain electrode materials such as LFP, a voltage plateau, resulting from two-phase coexistence, is shown in both charge and discharge cycles. The coexisting two phases are the lithium-deficient phase ($Li_{\alpha}FePO_4$) and the lithium-rich phase ($Li_{1-\beta}FePO_4$).

Plenty of approaches have been made to model phase-change phenomenon of LFP particles. Srinivasan and Newman [7] developed a core-shell model, which assumed the juxtaposition of two phases as a shrinking core, to simulate discharge behaviors for both half and full cells. It neglected the single-phase region at the beginning of discharge with the assumption of concentration-independent diffusion coefficients. The interface between two phases was located at the equilibrium concentration. A model was proposed by Wang et al. [8], in which the rate of phase transformation, lithium-ion diffusion in lithium-rich phase and the two-phase interface mobility were considered. A rectangular geometry of LFP particles, instead of spherical geometry, was applied in the model. Based on the previous model, Kavasajjula et al. [9] took the lithium-ion diffusion in lithium-deficient phase into consideration as well. The above models were only used to simulate discharge behaviors. A. Khandelwal et al.

[10] improved the shrinking-core model by Landau transformation to obtain a generalized moving boundary so that it could be used to investigate charge behaviors of LFP cells as well.

In recent years, phase field models based on non-equilibrium thermodynamics [11] have been proposed to understand phase transformation phenomenon on the level of nanoparticles quantitatively. A simplified equation derived from Cahn-Hilliard-Reaction (CHR) system by the work of Cahn and Hilliard [12] was presented by Singh et al. [13]. Bazant [14] incorporated Butler-Volmer kinetics into CHR model. Regardless of its usefulness of detailed understanding of the physical principles, phase field models are difficult to translate to the onboard algorithms.

In an alternate point of view, without physical multi-phase boundaries, concentration-dependent diffusion coefficients were introduced by many researchers. Thorat et al. [15] proposed a model to imitate phase-change behaviors by the concentration-dependent solid diffusion coefficients with consideration of thermodynamics under mass transport equations. It also took carbon coating and lithium diffusion in only one of the lattice dimensions into account. Based on the concept of concentration-dependent diffusivity, the particle-size distribution within electrodes was added into the model by Farkhondeh and Delacourt [16]. However, the model was limited at rates up to 1C due to the ignorance of electrolyte influences. Safari and Delacourt [17–18] also modeled the phase-change behavior with concentration-dependent diffusion coefficients albeit of an empirical origin on the basis of the resistive-reactant concept. The model was validated by an LFP half-cell and a commercial LFP/C cell, respectively. Even though it made a good agreement with experiments, the dependence on experimental results was still a limiting factor, because some transport parameters were obtained through experimental fitting methods.

In order to translate the physics-based electrochemical model to the onboard algorithm, plenty of reduction methods have been applied by researchers. The ROMs are aimed to increase computational efficiency and remain the accuracy to the most extend at the same time, which contain single particle model (SPM) [17], enhanced single particle model [19–20], state-variable model [21], reformulated model [22], and the proper orthogonal decomposition (POD) [23] model. The SPMs are limited to small currents, in which the electrolyte potential and concentration of electrolyte phase are neglected. For enhanced SPMs, electrolyte effects are considered by Galerkin approximation [19] or parabolic approximation [20]. The state-variable model successfully reduced 1/20 computational time than full order model (FOM) by residue grouping. Initial guesses were necessary for the reformulated model and POD model. Aside from the numerical reduction methods mentioned above, Kumar [24] proposed another physics-based methodology of volume averaging to accomplish order reduction of the electrochemical equations. Since the reduction methods have an assumption of the uniform reaction rate, the volume averaging is only applicable to constant charge/discharge profiles.

Investigations about degradation mechanism are conducted by both stored and used lithium-ion batteries, which are related to calendar life and cycle life, respectively. The degradation of cells in storage is dominated by its self-discharge rate, while that of cells in usage is mainly governed by side reactions [25, 26, 27, 28, 29, 30, 31, 32, 33, 34, 35, 36, 37] occurring at the composite anode. Lithium ions and electrolyte take side reactions at the interface between electrode and electrolyte, resulting in the generation of organic and inorganic products, which are the components of the solid electrolyte interphase (SEI). Capacity fade and impedance rise are two main effects of degradation. Capacity fade mainly corresponds to the loss of lithium ions and loss of active materials, while impedance rise, resulting in power fade, corresponds to the SEI increment and electrolyte reduction.

The degradation study of LFP cells was firstly introduced by Striebel et al. [38] in 2003. The 1.6mAh LFP/graphite cells were stored and cycled at 25°C for a short period. It concluded that the capacity fade and power fade were arisen from lithium ions consumption and the growth of SEI, respectively. Then Striebel et al. [39] continued to study the aging mechanism of LFP/graphite cells with two different electrolyte salts, $LiPF_6$ and LiBOB, cycling at 25°C. It was observed that the capacity fade in $LiPF_6$ was two times more than that in LiBOB. Material analysis verified the existence of deposited Fe on the anode surface. It also proposed that the iron deposition on anode catalyzed the SEI formation. Zaghib et al. [40] proposed that the iron deposition on anode was caused by the Fe impurities on the cathode. Until 2009, the commercial cylindrical LFP/graphite cells (nominal capacity: 1.45Ah) were firstly cycled at 25°C for about 600 cycles by Dubarry et al. [41]. M. Safari et al. [33] experimentally investigated aging mechanism of 2.3Ah commercial LFP based cells both in storage and usage thoroughly. Differential analysis was used to analyze characteristics of the aged cells. It revealed that high temperature could accelerate the degradation of cells.

Most analysis of degradation is limited to experiments, especially for LFP based lithium ion batteries. In this paper, the ROM based on electrochemical thermal principles was developed at first. Then based on the developed ROM, degradation effects were incorporated to develop a semi-empirical degradation model.

EXPERIMENTS

Experiments for fresh and cycled cells were proceeded by the large format pouch type LFP/graphite cells. The cells are composed of a carbon-coated $LiFePO_4$ cathode and a graphite anode, with the nominal capacity of 20Ah. The cutoff voltages allowed by the manufacturer for charging and discharging are 3.6V and 2.5V, respectively. All the experiments were conducted in a thermal chamber, which was treated as a temperature controller. K-type thermocouples were adhesive to the surface of cells to measure battery surface temperatures. A programmable power supply (Sorensen DCS8-125E) and a programmable electric-load (KIKUSUI PLZ1004W) were connected in parallel to the battery to generate charging and discharging current profiles. Electrochemical impedance spectroscopy (EIS) measurement and parameter extraction were performed by GAMRY.

Experiments of fresh cells include open-circuit voltage (OCV) measurements, baseline data collection, and the existence of path dependence verification. OCV measurement was performed at a very small current of 0.05C-rate (1A) at an ambient temperature of 25°C. The protocol of baseline data collection was as follows: 1) pre-tests: 5 initial discharge/charge cycles were conducted by 1C-rate (20A) current, with 30 minutes rest between each consecutive discharge and charge cycle; 2) baseline tests: 4 full-range discharge/charge cycles were performed at different ambient temperature (25°C, 35°C, and 45°C, respectively) of different current, 0.1C, 1C, 3C, and 4C, respectively. The time interval for rest between each discharge and charge process was 30 minutes. The experimental evidence of the existence of path dependence shows that the electrochemical behaviors of LFP cells are dependent on their cycling history. [42] Two experimental paths were used to demonstrate the existence of path dependence of LFP cells. Path 1 and path 2 corresponded to (a) and (b) shown in Fig. 5, respectively. Path 1: (1) charge a fully discharged cell to achieve 50% SOC at 1/20C; (2) rest 2h; (3) continue to charge the cell to 100% SOC at 1C. Path 2: (1) discharge a fully charged cell to reach 50% SOC at 1/20C; (2) rest 2h; (3) charge the cell to 100% SOC at 1C.

Aging experiments were conducted by 5 pouch type LFP/graphite cells. The cells are cycled at different temperatures (25°C, 45°C) and SOC ranges (5-75%, 25-95%). In order to accelerate the aging tests, high discharge and charge current (4C, 80A) were applied to the cells. The tests were interrupted every 30 or 40 cycles for characterization tests, including capacity and EIS measurements. The capacity was measured at 0.5C (10A) in four steps: (1) fully charge at a constant current of 1C; (2) keep constant voltage until cutoff current of 0.4A; (3) 30 minutes rest; (4) fully discharge at 0.5C. The frequency range for EIS measurement was from 1kHz to 10mHz.

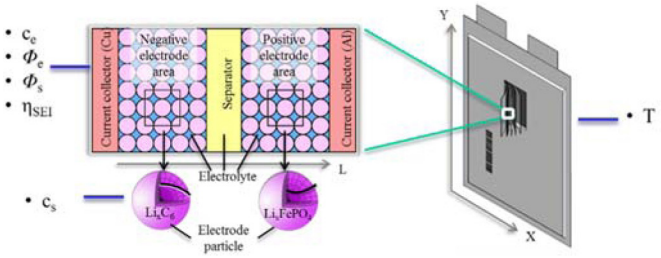

Fig. 1. Model set-up for a pouch type single cell and a microcell [43].

ROM AND SEMI-EMPIRICAL DEGRADATION MODEL

ROM

A pouch type LFP/graphite lithium ion battery is constructed by layers of electrode, separator and current collectors. Every single cell is composed of many microcells, as shown in Fig. 1. A sandwich structured microcell, which has a separator in the middle of a composite negative electrode and a composite positive electrode, is the basic element used to model characteristics of lithium ion batteries. During charge and discharge processes, the lithium ions shuttle back and forth between the composite anode and the composite cathode. In the FOM, ion transportation, diffusion, intercalation/deintercalation processes are solved by several partial differential equations (PDEs). The ion concentration in electrode and electrolyte, the potential of electrode and electrolyte are governed by Fick's law and Ohm's law, respectively. The electrochemical kinetics are governed by Butler-Volmer equation.

Even though the FOM could obtain accurate enough results, it is still a time consuming method. It is necessary to simplify the governing equations used in the FOM by some reduction techniques. Table 1 summarizes the governing equations and their boundary conditions for the FOM. Table 2 shows the applied reduction methods and the simplified governing equations for the ROM. Polynomial approach and state space approach were used to simplify equations of ion concentration in electrode and electrolyte, respectively. Butler-Volmer equation, taking both a cathodic and an anodic reaction into consideration, was linearized to reduce the calculation time of current density. As for the characteristics of two-phase transition and existence of path dependence, the ROM should be modified with consideration of the number of layers coexisting in the positive electrode particles. The order of equations for ion concentration at the inner layer of particles was reduced by a biquadratic polynomial, while that at outer layer was reduced by a quadratic polynomial. Table 3 shows the governing equations for ion concentration in the solid particles.

Semi-Empirical Degradation Model

Side reaction is the predominant cause of degradation for lithium ion batteries, which has been widely accepted in recent years. The effects of side reactions include loss of ions, loss of active materials, electrolyte reduction, and SEI formation. The schematic diagram of degradation process happened on anode is shown in Fig. 2. The yellow color areas represent the byproducts of side reactions. SEI are the byproducts located at the interface between electrode particle and electrolyte, partially or fully covered the surface of particles. The byproducts accumulated between composite anode and separator, adhesive to the separator, are defined as the deposit layer. The particles with marker 'X' are treated as the isolated particles which are fully covered by SEI.

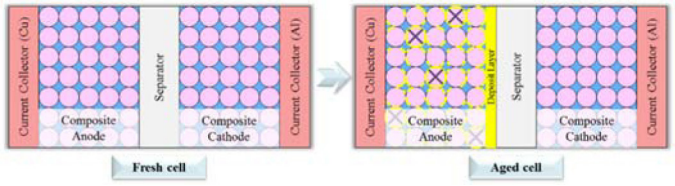

Fig. 2. Schematic diagram of degradation processes taking place at anode.

SEI is conductive to lithium ions, but isolative to electrons, which barriers chemical reactions at the covered surface of anode particles. When the particle is fully covered by SEI, it is completely inaccessible for electrons, which stops all chemical reactions taking place. With the increase of the number of cycles, lithium ions are continuously consumed due to side reactions. More active area on the surface of anode particles is covered by SEI, which causes the losses of active material. Electrolyte consumption in side reactions increases the electrolyte resistance, which causes power fade.

Based on the degradation mechanism mentioned above, four parameters, volume fraction of active anode material, SEI resistance, the resistance of deposit layer and electrolyte diffusion coefficient, can be used to describe the degradation effects of loss of active material, the growth of SEI, the growth of deposit layer, and electrolyte decomposition, respectively. Table 4 summarizes the identification of degradation parameters.

RESULTS AND DISCUSSION

Experimental Analysis of Both Fresh and Cycled Cells

Charging and Discharging Behaviors for Fresh Cells

Charging and discharging behaviors are the basic characteristics of lithium ion batteries. The two-phase transition is represented as the voltage plateau in the voltage profiles. Fig. 3 shows the voltage profiles of charging and discharging of LFP/graphite cells at different current densities. Two apparent features are shown as follows: (1) asymmetric potential behaviors between discharge and charge, known as hysteresis; (2) charge capacity is larger than discharge capacity, especially in low current. It reveals that the utilization on charge is higher than that on discharge.

Table 1. Governing equations for the FOM

	FOM	
Ion concentration in electrode	$\frac{\partial c_s}{\partial t}=\frac{D_{s,\alpha}}{r^2}\frac{\partial}{\partial r}\left(r^2\frac{\partial c_s}{\partial r}\right);\ \frac{\partial c_s}{\partial t}=\frac{D_{s,\beta}}{r^2}\frac{\partial}{\partial r}\left(r^2\frac{\partial c_s}{\partial r}\right);$ B.C.: $D_{s,\beta}\frac{\partial c_s}{\partial r}\Big\|_{r=r_1}=0, D_{s,\alpha}\frac{\partial c_s}{\partial r}\Big\|_{r=R_s}=\frac{-j^{Li}}{a_s F}$ $\left(c_{s,\alpha\beta}-c_{s,\beta\alpha}\right)\frac{\mathrm{d}r_0}{\mathrm{d}t}=D_{s,\beta}\frac{\partial c_{s,\beta}}{\partial r}\Big\|_{r=r_0}-D_{s,\alpha}\frac{\partial c_{s,\alpha}}{\partial r}\Big\|_{r=r_0}$	(1)
Ion concentration in electrolyte	$\frac{\partial(\varepsilon_e c_e)}{\partial t}=\frac{\partial}{\partial x}\left(D_e^{\mathrm{eff}}\frac{\partial}{\partial x}c_e\right)+\frac{1-t_+^0}{F}j^{\mathrm{Li}}$ B.C.: $\frac{\partial c_e}{\partial t}\Big\|_{x=0}=\frac{\partial c_e}{\partial t}\Big\|_{x=L}=0$	(2)
Ohm's law in electrode	$\frac{\partial}{\partial x}\left(\sigma^{\mathrm{eff}}\frac{\partial}{\partial x}\phi_s\right)-j^{\mathrm{Li}}=0$ B.C.: $-\sigma^{\mathrm{eff}}\frac{\partial}{\partial x}\phi_s\Big\|_{x=0}=-\sigma^{\mathrm{eff}}\frac{\partial}{\partial x}\phi_s\Big\|_{x=L}=\frac{I}{A};$ $\frac{\partial}{\partial x}\phi_s\Big\|_{x=L_-}=\frac{\partial}{\partial x}\phi_s\Big\|_{x=L_-+L_{\mathrm{sep}}}=0$	(3)
Ohm's law in electrolyte	$\frac{\partial}{\partial x}\left(\kappa^{\mathrm{eff}}\frac{\partial}{\partial x}\phi_e\right)+\frac{\partial}{\partial x}\left(\kappa_D^{\mathrm{eff}}\frac{\partial}{\partial x}\ln c_e\right)+j^{\mathrm{Li}}=0$ B.C.: $\frac{\partial}{\partial x}\phi_e\Big\|_{x=0}=\frac{\partial}{\partial x}\phi_e\Big\|_{x=L}=0$	(4)
Electrochemical kinetics	$j^{\mathrm{Li}}=a_s i_0\left\{\exp\left[\frac{\alpha_a F}{RT}(\eta-\eta_{\mathrm{SEI}})\right]-\exp\left[-\frac{\alpha_c F}{RT}(\eta-\eta_{\mathrm{SEI}})\right]\right\}$ $\eta=\phi_s-\phi_e-U$	(5)

Fig. 4 shows the schematic diagram of a shrinking-core model to describe phase transition during charge and discharge of LFP electrode. For discharge, lithium ions are extracted from anode particles, then transport from anode side to cathode side inside the cells, while electrons transport through the external circuit. At the surface of cathode particles, Li^+ and electrons take chemical reactions and then finally rest in the crystal structure. When discharge continues, more and more lithium ions move to cathode side so that the surface concentration of LFP particles has been increased. Until it reaches a certain value, a new phase, Li-rich phase, does begin to generate at the surface of Li-deficient phase. The LFP particles are composed of two layers, Li-deficient phase ($Li_\alpha FePO_4$) covered by Li-rich phase ($Li_{1-\beta}FePO_4$). It ends when the core is completely consumed. The process of the two-phase transition during charge proceeds in the opposite way, resulting in a core of Li-rich phase covered by a shell of Li-deficient phase.

Table 2. Applied reduction methods and governing equations for the ROM

Equation description	Reduction method	ROM	
Ion concentration in electrode	Polynomial approach	See Table 3	(6)
Ion concentration in electrolyte	State space approach	$\begin{cases}\dot{C}_e^* = A^*\cdot C_e + B^*\cdot i\\ C_e = C^*\cdot C_e + D^*\cdot i\end{cases}$	(7)
Ohm's law in electrode	Finite difference method (FDM)	$\frac{\partial}{\partial x}\left(\sigma^{\mathrm{eff}}\frac{\partial}{\partial x}\phi_s\right)-j^{\mathrm{Li}}=0$ $-\sigma^{\mathrm{eff}}\frac{\partial}{\partial x}\phi_s\Big\|_{x=0}=-\sigma^{\mathrm{eff}}\frac{\partial}{\partial x}\phi_s\Big\|_{x=L}$ $=\frac{I}{A};\frac{\partial}{\partial x}\phi_s\Big\|_{x=L_-}=\frac{\partial}{\partial x}\phi_s\Big\|_{x=L_-+L_{\mathrm{sep}}}=0$	(8)
Ohm's law in electrolyte	Ce has no influence on reaction current $\frac{\partial}{\partial x}\left(k_D^{\mathrm{eff}}\frac{\partial}{\partial x}\ln c_e\right)=0$	$\frac{\partial}{\partial x}\left(\kappa^{\mathrm{eff}}\frac{\partial}{\partial x}\phi_e\right)+j^{\mathrm{Li}}=0$	(9)
Electrochemical kinetics	Linearization	$\frac{\partial}{\partial x}\left(\frac{\partial}{\partial x}\phi_s-e\right)=j^{Li}\left(\frac{1}{\sigma^{eff}}+\frac{1}{k^{eff}}\right)$ $j^{Li}=\frac{a_s i_0 F}{RT}(\phi_s-e-U)$	(10)

Table 3. Simplified governing equations for ion concentration in solid phase by polynomial approaches

	ROM equations	
Cs,surf	$\frac{\left(C_{s,\mathrm{surf}}-C_{s,\beta\alpha}\right)\left(k_2-2k_1(r_s-r_0)\right)}{k_2k_3-k_1k_4}$ $-\frac{\left(C_{s,\mathrm{ave}}-C_{s,\beta\alpha}\right)\left(2k_3(r_s-r_0)-k_4\right)}{k_2k_3-k_1k_4}=\frac{-j^{Li}}{a_s F}$	(11)
Cs,ave of outer layer	$C_{s,ave0}^{k+1}\frac{4}{3}\pi\left(r_s^3-\left(r_0^{k+1}\right)^3\right)-C_{s,ave0}^{k}\frac{4}{3}\pi\left(r_s^3-\left(r_0^{k}\right)^3\right)$ $+C_{s,ave1}^{k+1}\frac{4}{3}\pi\left(r_0^{k+1}\right)^3-C_{s,ave1}^{k}\frac{4}{3}\pi\left(r_0^{k}\right)^3=\frac{-j^{Li}}{a_s F}4\pi r_s^2$	(12)
Interface	$\left(C_{s,\beta\alpha}-C_{s,\alpha\beta}\right)\frac{\mathrm{d}r_0}{\mathrm{d}t}$ $=-D_{s,\beta}\frac{\left(C_{s,\mathrm{surf}}-C_{s,\beta\alpha}\right)k_2-\left(C_{s,\mathrm{ave}}-C_{s,\beta\alpha}\right)k_4}{k_2k_3-k_1k_4}$ $+\frac{D_s}{r_0}\left(35\left(c_{s,\mathrm{surf}}-c_{s,\mathrm{ave}}\right)-8q_{\mathrm{ave}}r_0\right)$	(13)
Cs,ave of inner layer	$\frac{d}{dt}c_{s,\mathrm{ave}}-3\frac{D_s}{r_0^2}\left(35\left(c_{s,\mathrm{surf}}-c_{s,\mathrm{ave}}\right)-8q_{\mathrm{ave}}r_0\right)=0$	(14)
q_{ave} of inner layer	$\frac{d}{dt}q_{\mathrm{ave}}+\frac{1}{2}\frac{D_s}{r_0^3}\left(60q_{\mathrm{ave}}r_0-45\right)\left(35\left(c_{s,\mathrm{surf}}-c_{s,\mathrm{ave}}\right)-8q_{\mathrm{ave}}r_0\right)$ $=0$	(15)

Table 4. Identification of degradation parameters

	Equations	
Side reaction	$j_{side}^{Li} = -i_{0,side} a_s \exp(-\frac{\alpha_{c,side} n_{side} F}{RT} \eta_{side})$ $\eta_{side} = \phi_s - \phi_e - U_{eq,side} - \frac{R_{SEI}}{a_{s-}}(j^{Li} + j_{side}^{Li})$	(16)
Loss of active material	$a_{s-} = \frac{4\pi r_s^2}{4/3\pi r_s^3}, \varepsilon_{s-} = 3\frac{\varepsilon_{s-}}{r_s}$	(17)
Growth of SEI Growth of deposit layer	$R_{SEI+DL} = \frac{R_{SEI}}{a_{s-}\delta_-} + R_{DL}$	(18)
Electrolyte decomposition	$D_e^{eff} = D_e \cdot \varepsilon_e$	(19)

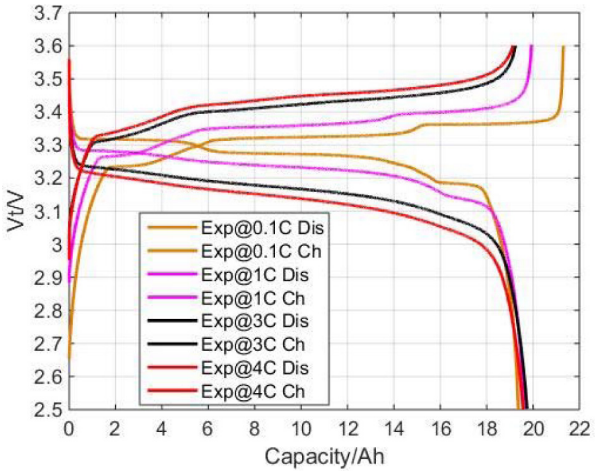

Fig. 3. Asymmetry between discharge and charge behaviors of LFP/graphite cells at 25°C.

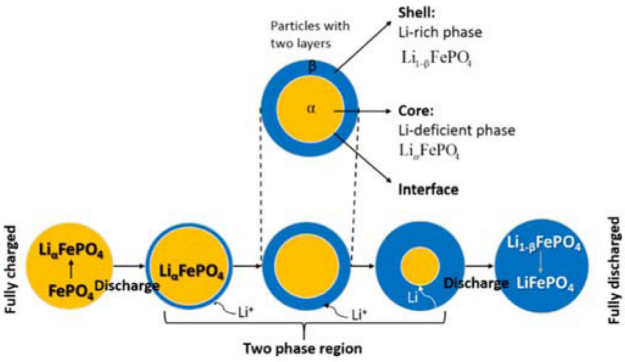

Fig. 4. Schematic diagram of a shrinking-core model to describe phase separation of $LiFePO_4$ electrode.

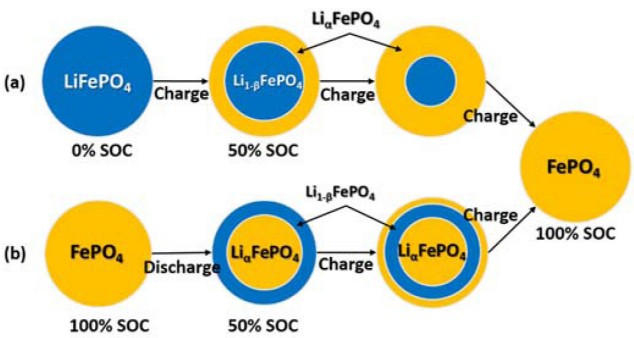

Fig. 5. Schematic diagram of the juxtaposition of phases in LFP particles at different SOCs with different cycling history: blue and yellow color for β and α phase, respectively.

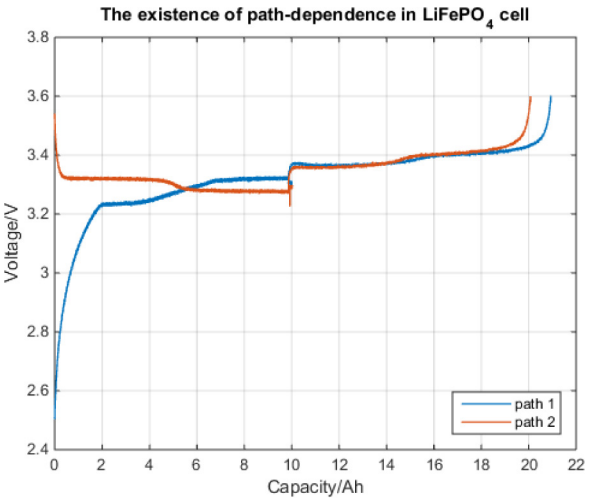

Fig. 6. Experimental evidence of the existence of path-dependence in LFP cathode.

Experimental Evidence of Existence of Path Dependence

The schematic diagram of the shrinking-core model used to describe the juxtaposition of phases in LFP electrode is shown in Fig. 5. The blue and yellow color represents lithium-rich phase (β phase) and lithium-deficient phase (α phase) of LFP particles, respectively. The experimental evidence of the existence of path dependence is shown in Fig. 6, in which the blue and orange lines relate to path 1 and path 2, respectively. At the beginning of path 1, only β phase exists in the fully discharged particles. As the charging process goes by, the lithium ions transport from the cathode side to the anode side, which results in the decrease of the surface ion concentration of LFP particles. When the surface ion concentration decreases to a critical value, a new phase, α phase, becomes to generate on the surface of LFP particles. When charging continues, more and more lithium ions are extracted through the two-phase interface to the surface of particles. Due to the moving boundary, α phase on the shell expands while β phase in the core shrinks. The core is completely consumed at the end of charging, with only α phase existing in the LFP particles.

Table 5. Test matrix

Cell No.	Temp.	Cha./Dis.	ΔSOC	Cycle No.	Capacity fade
16	25°C	4C/4C	5%-75%	200	5.81%
15				240	10.95%
10			25%-95%	270	14.17%
20	45°C			150	12.17%
18				180	23.54%

In path 2, the cell is discharged from the fully charged state. The process described above happened in the opposite way, which results in the formation of core-shell particles, α phase in the core and β phase on the shell. Then the cell is charged from 50% SOC to 100% SOC. A new lithium-deficient phase, α phase, generates at the surface of particles when the surface lithium ion concentration decreases to a critical value. As charging proceeds, lithium ions transport from the surface through the new lithium-deficient phase to the interface between new α phase and β phase, which results in the formation of three-phase coexisting particles with two interfaces. Charging continues until the core is consumed completely.

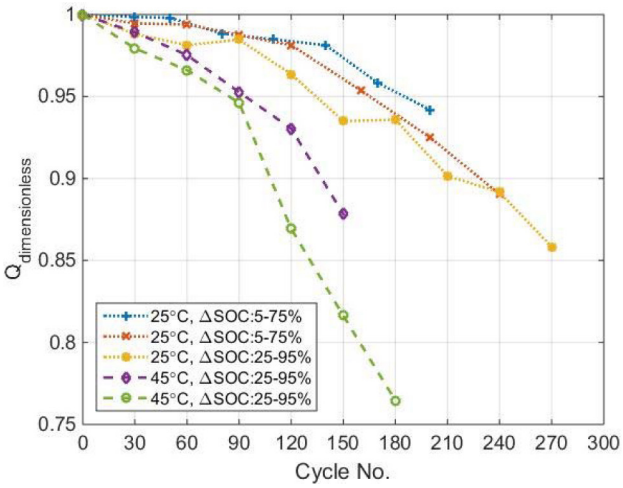

Fig. 7. Dimensionless capacity vs. cycle number at different temperatures and SOC cycling range.

According to the experimental results shown in Fig. 6, the juxtaposition of phases depends on the cycling history of LFP cells. Capacity results are different when the experiments are aimed to reach the same SOC through different paths. When the cell is charged from a fully discharged state as shown in path 1, a core of β phase covered by a shell of α phase is shrunk because of continuous extraction of lithium ions from the core. The diffusion distance through α phase for lithium ions is increased. On the other way, the cell is discharged from a fully charged state to 50% SOC, with a core of α phase covered by a shell of β phase. When it is charged further, the old shell of β phase will be covered by the newly generated α phase. In this case, the diffusion can only be through the new shell of α phase. The diffusion distance is relatively shorter than that in path 1, which causes the difference in final capacity.

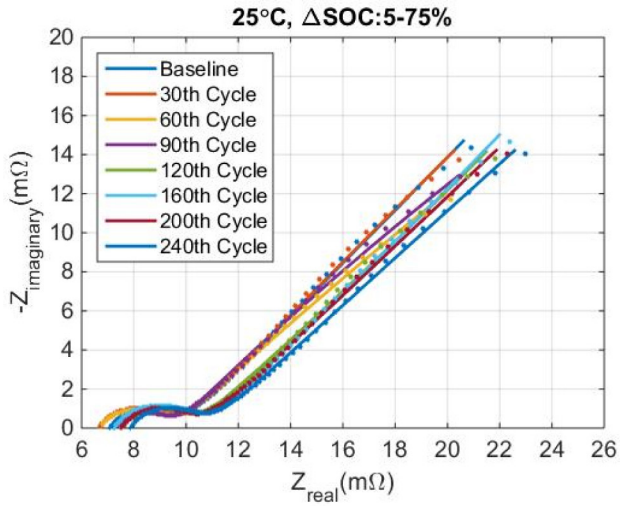

Fig. 8. Electrochemical impedance spectra of the cell cycling at 25°C by SOC cycling range from 5% to 75%.

Capacity Fade Analysis of Cycled Cells

In order to study the degradation mechanism for pouch type LFP/graphite cells, it is necessary to take accelerated tests to shorten the time to reach the end of life. A high charge/discharge current of 80A was applied to do cycling tests. Temperature, SOC cycling range, and cycle number haven been considered to investigate their influence on cells degradation. The test matrix is summarized in Table 5.

Capacity, Q_{max}, was measured at 0.5C (10A) every 30 or 40 cycles. The capacity fade of five commercial pouch type lithium ion batteries at different operating conditions were 5.81%, 10.95%, 14.17%, 12.17%, and 23.54%, respectively. Since the initial capacity measured at different temperature is different, a dimensionless capacity retention, $Q_{dimensionless}$ is introduced and defined as the capacity ratio of an aged cell over a fresh cell.

$$Q_{dimensionless} = \frac{Q_{aged\ cell}}{Q_{fresh\ cell}} \tag{20}$$

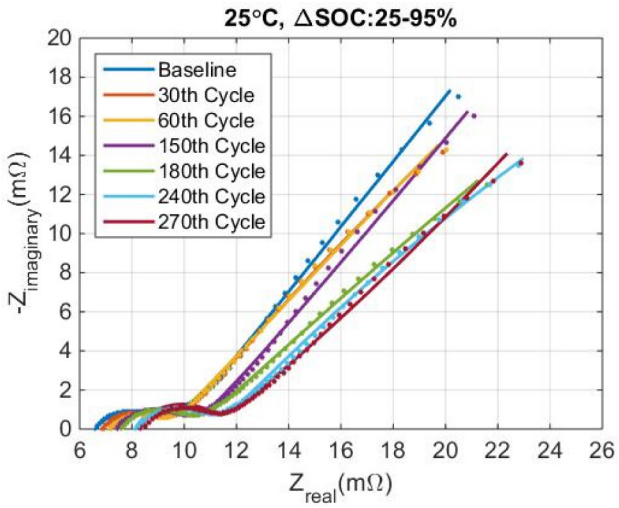

Fig. 9. Electrochemical impedance spectra of the cell cycling at 25°C by SOC cycling range from 25% to 95%.

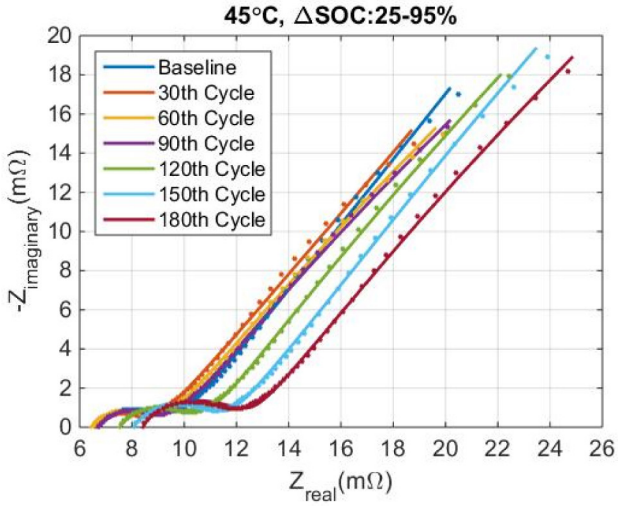

Fig. 10. Electrochemical impedance spectra of the cell cycling at 45°C by SOC cycling range from 25% to 95%.

The dimensionless capacity retentions at different operating conditions are plotted in Fig. 7. The markers on the dotted line are of cells cycling under 25°C, while those on dashed lines are of cells cycling under 45°C. Generally speaking, the capacity decreased as

the cycle number increased. The decreasing rate of capacity is relatively slow at the beginning and then aggravated after reaching a certain amount of capacity fade. It also illustrates that high temperature can accelerate degradation to cause more capacity fade. Compared with the influence of temperature on the capacity fade, that of SOC cycling range is not obvious.

EIS Analysis of Cycled Cells

The impedance characteristics of LFP/graphite cells were measured by electrochemical impedance spectroscopy (EIS) every 30 or 40 cycles at different operating conditions, shown from Fig. 8 to Fig. 10. The dots in Nyquist plots are measured data by EIS, while the solid lines are fitted data by the equivalent circuit model (ECM).

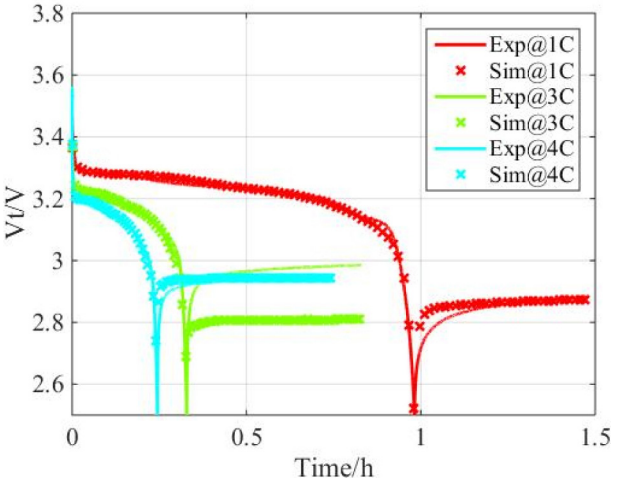

Fig. 11. Comparison of terminal voltage between simulation results of the ROM and experimental data with 1/3/4C discharging current applied.

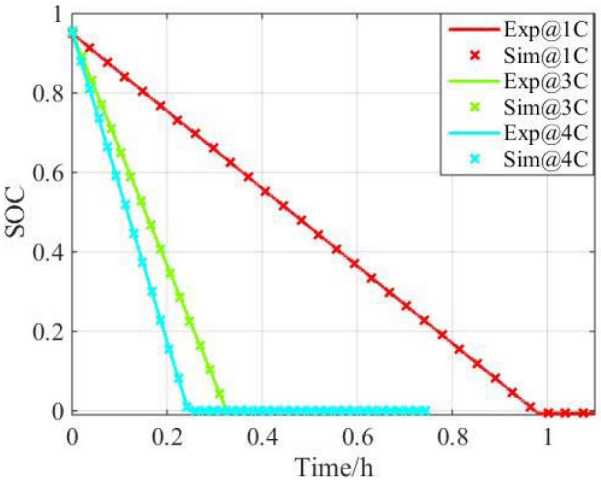

Fig. 12. Comparison of terminal voltage between simulation results of the ROM and experimental data with 1/3/4C discharging current applied.

The electrochemical impedance spectra are composed of an obvious semi-circle, an unobvious semi-circle, and a slope line. The first obvious semi-circle corresponds to an RC circuit in ECM, representing SEI resistance and capacitance in high frequencies. The second unobvious semi-circle is also related to an RC circuit in the ECM, in charge of charge transfer resistance and double layer capacitance in medium frequencies. The slope line dominates the characteristics in low frequencies, relating to a series connection between Warburg resistance and intercalation capacitance in the ECM. Compared the electrochemical impedance spectra at different cycling conditions with each other, high temperature and high SOC cycling range cause more impedance rise. High SOC cycling range has a less obvious influence on capacity fade than on power fade resulting from impedance rise.

Validation of the ROM and Semi-Empirical Degradation Model

ROM Validation for Fresh Cells

In order to verify the accuracy of the ROM, experimental data of charging and discharging profiles with resting included for commercial cells were collected and compared with simulation results. The parameters of instinct characteristics of cells, such as geometric and morphologic ones, were provided by manufactures. Others were initially obtained from the literature and then optimized by validation. The equilibrium potentials of both cathode and anode were estimated by empirical equations and then optimized based on the measured OCV-SOC data. The commercial pouch type LFP/graphite cells were charged and discharged at different C-rate (1/3/4C) under an ambient temperature of 25°C. The comparison results of terminal voltage and SOC between experiments and simulations results are displayed from Fig. 11 to Fig. 14. The solid lines and markers in the figures represent experimental data and simulation results, respectively. The simulated response of terminal voltage and SOC during discharge/charge with rest involved shows great consistency with experimental data. However, the discrepancy existed in voltage profiles in resting period when a 3C discharging current was applied to the cells.

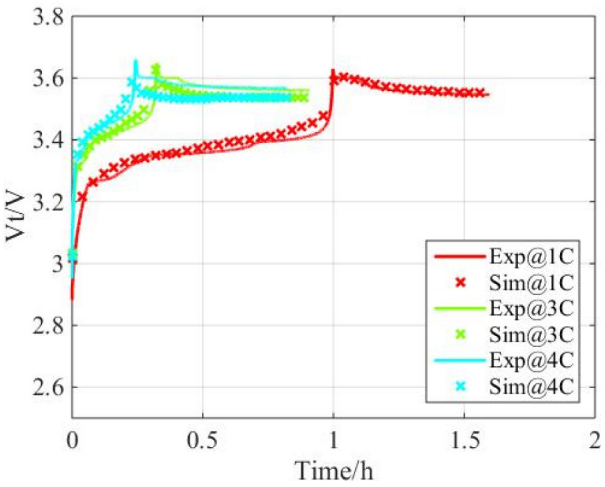

Fig. 13. Comparison of terminal voltage between simulation results of the ROM and experimental data with 1/3/4C charging current applied.

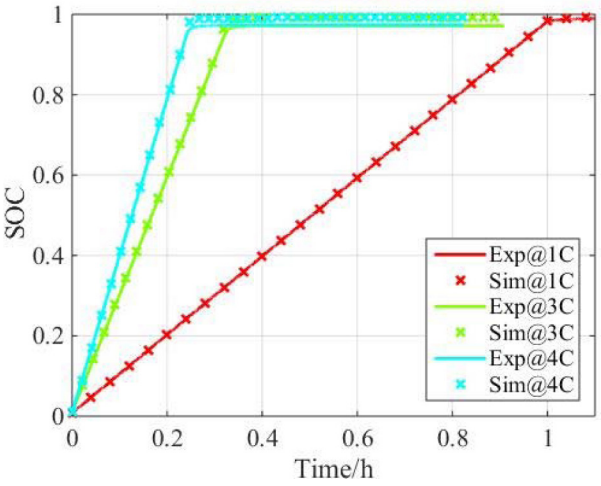

Fig. 14. Comparison of terminal voltage between simulation results of the ROM and experimental data with 1/3/4C charging current applied.

Average ion concentration of electrode particles was used to conduct SOC estimation, while Coulomb counting was the method for SOC measurement. Since constant current was applied to the cells, the slope of SOC estimation curve was a constant. Based on the comparison results plotted in Fig. 12 and Fig. 14, SOC estimation by the ROM had a fairly good match with experimental results.

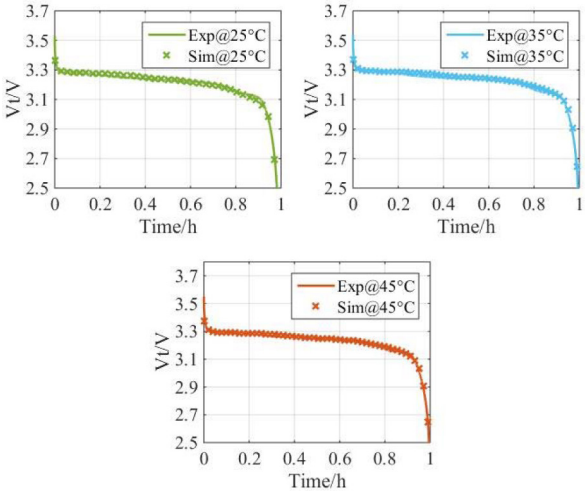

Fig. 15. Comparison of terminal voltage between simulation results of the ROM and experimental data with 1C discharging current applied at different ambient temperatures (25°C, 35°C, and 45°C).

Some parameters in the ROM can be highly affected by temperatures, such as diffusion coefficients in electrode and electrolyte. Based on the analysis of parameter sensitivity, the diffusion coefficient in solid phase had an influence on capacity, while that in solution phase could affect overpotential. Then those temperature-dependency parameters were fitted by Arrhenius equation. 1C discharge current was applied to the large format pouch type cells at different ambient temperatures (25°C, 35°C, and 45°C). The testing condition was chosen as an example to test the reliability of the ROM. The comparison of terminal voltage and SOC between simulation results of the ROM and experimental data under exampled operating condition are shown in Fig. 15 and Fig. 16. Both terminal voltage and SOC estimation show good consistency with experiments.

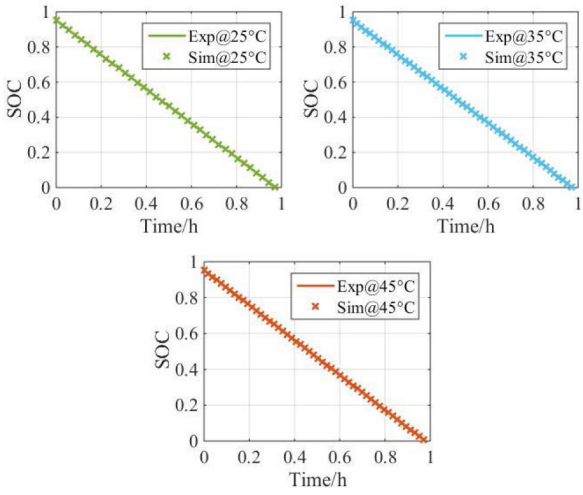

Fig. 16. Comparison of SOC between simulation results of the ROM and experimental data with 1C discharging current applied at different ambient temperatures (25°C, 35°C, and 45°C).

Validation of the Semi-Empirical Degradation Model

The commercial LFP/graphite cells were cycled under highly accelerated testing conditions. With the increase of cycle numbers, the capacity decreased resulting from ion loss and active material loss. Power fade comes from the growth of SEI, deposit layer, and electrolyte reduction. According to the degradation mechanism aforementioned, there are three key parameters, the volume fraction of active anode material, the combined resistance of SEI and deposit layer, and the effective electrolyte diffusion coefficient in the semi-empirical degradation model. The extraction of the key parameters was based on the nonlinear least square method.

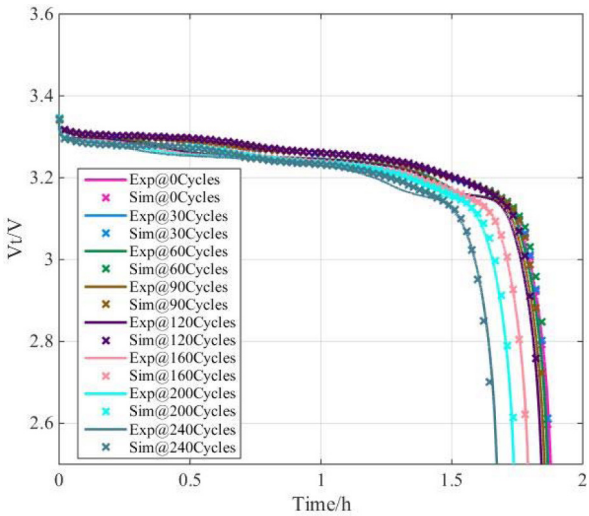

Fig. 17. Comparison of terminal voltage between simulations by the semi-empirical degradation model and experiments as a function of cycle numbers at 25°C.

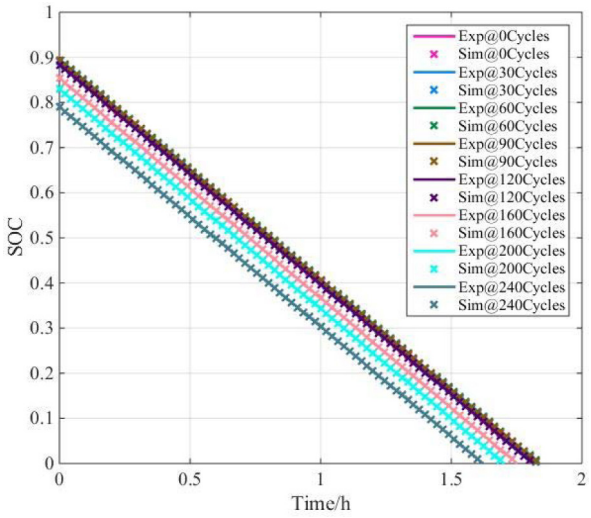

Fig. 18. Comparison of SOC between simulations by the semi-empirical degradation model and experiments as a function of cycle numbers at 25°C.

The comparison of the terminal voltage between simulations by the semi-empirical degradation model and experiments as a function of cycle numbers at the ambient temperature of 25°C is plotted in Fig. 17. As the cells degraded, the time to reach discharge cutoff voltage was decreased. SOC estimation by semi-empirical degradation model was compared with Coulomb counting experimental results at different cycle numbers at 25°C, the results of which are depicted in Fig. 18. The utilization window of SOC is shrunk due to the capacity loss in the degradation process of LFP/graphite cells.

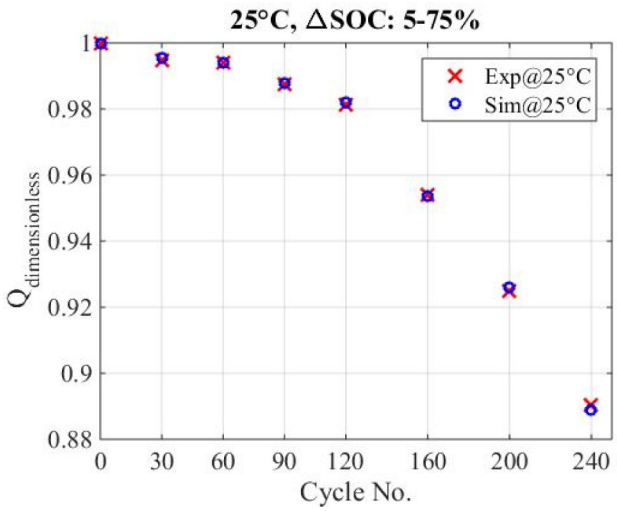

Fig. 19. Comparison of capacity estimated by semi-empirical degradation model and experimental measurements at 25°C.

Capacity fade is one of the most significant criteria to evaluate the degraded condition of lithium ion batteries. The comparison of capacity estimated by the semi-empirical degradation model and experimental measurements is figured in Fig. 19. The error of capacity calculation is within 0.2%.

Based on the comparison results shown above, the semi-empirical degradation model incorporated into a developed ROM shows good performance for cycled cells at 25°C. However, it is still an unpredictable method due to its high dependence on experimental data, which limits its range of application. Therefore, a physics based degradation model incorporated into the ROM will be developed in the future work to eliminate the limitations of the semi-empirical degradation model.

CONCLUSIONS

The ROM and semi-empirical degradation model have been developed and validated for pouch type LFP/graphite lithium ion batteries. Experimental investigation of 20Ah LFP/graphite were conducted for both fresh and cycled cells. A shrinking-core model was used to model the characteristics of LFP/graphite cells, including two-phase transition and path dependence. The existence of path dependence for LFP based cells was verified by experiments. Five cells were cycled under different operating conditions, including different temperatures, SOC cycling ranges, and cycle numbers. A shrinking-core model was used to model characteristics of LFP/graphite cells, including two-phase transition and path dependence. The temperature dependent parameters, such as diffusion coefficient in electrode and electrolyte, were fitted by Arrhenius equation. The comparison of the response of terminal voltage and SOC between simulation results by the ROM and the collected experimental data shows good consistency.

Side reaction is regarded as the predominant factor of degradation for LFP/graphite lithium ion batteries. Capacity fade and impedance rise are two key consequences after cells getting aged. Capacity fade mainly corresponds to the loss of lithium ions and loss of active materials, while impedance rise, resulting in power fade, is related to the growth of SEI, deposit layer and electrolyte consumption in side reaction. Capacity and EIS results manifest that elevated temperature and high SOC cycling range could accelerate degradation process. In order to develop a semi-empirical degradation model, three key parameters, the volume fraction of the active material, the combined resistance of SEI and deposit layer, and the effective electrolyte diffusion coefficient, were extracted from experimental data by the nonlinear least square method. The error of capacity estimation was limited within 0.2%. The semi-empirical degradation model was limited by its high dependency on experimental data. Therefore, a physics based electrochemical degradation model should be developed to accomplish the prediction of capacity fade in the future work.

REFERENCES

1. Padhi, A. K., Nanjundaswamy, K. S., Masquelier, C., Okada, S. ., "Effect of structure on the Fe^{3+}/Fe^{2+} redox couple in iron phosphates." *Journal of the Electrochemical Society* 144, no. 5 (1997): 1609–1613. doi:10.1149/1.1837649
2. Ritchie, A. and Howard, W., "Recent developments and likely advances in lithium-ion batteries." *Journal of Power Sources* 162, no. 2 (2006): 809–812.
3. Wood, E., Alexander, M. and Bradley, T.H., "Investigation of battery end-of-life conditions for plug-in hybrid electric vehicles." *Journal of Power Sources*196, no. 11 (2011): 5147–5154.
4. Zackrisson, M., Avellán, L. and Orlenius, J., "Life cycle assessment of lithium-ion batteries for plug-in hybrid electric vehicles–Critical issues." Journal of Cleaner Production 18, no. 15 (2010): 1519–1529.
5. Gambhire, P., Hariharan, K.S., Khandelwal, A., Kolake, S.M. ., "A physics based reduced order aging model for lithium-ion cells with phase change." Journal of Power Sources 270 (2014): 281–291.

6. Doyle, M., Fuller, T.F. and Newman, J., "Modeling of galvanostatic charge and discharge of the lithium/polymer/insertion cell." *Journal of the Electrochemical Society* 140, no. 6 (1993): 1526–1533. doi:10.1149/1.2221597
7. Srinivasan, V. and Newman, J., "Discharge model for the lithium iron-phosphate electrode." Journal of the Electrochemical Society 151, no. 10 (2004): A1517–A1529. doi:10.1149/1.1785012
8. Wang, C., Kasavajjula, U.S. and Arce, P.E., "A discharge model for phase transformation electrodes: formulation, experimental validation, and analysis." The Journal of Physical Chemistry C 111, no. 44 (2007): 16656–16663. doi:10.1149/1.2980420
9. Kasavajjula, U.S., Wang, C. and Arce, P.E., "Discharge model for $LiFePO_4$ accounting for the solid solution range." Journal of the Electrochemical Society 155, no. 11 (2008): A866–A874.
10. Khandelwal, A., Hariharan, K.S., Kumar, V.S., Gambhire, P. ., "Generalized moving boundary model for charge–discharge of $LiFePO_4$/C cells." Journal of Power Sources 248 (2014): 101–114.
11. Bazant, M. Z. "Theory of chemical kinetics and charge transfer based on nonequilibrium thermodynamics." Accounts of chemical research 46, no. 5 (2013): 1144–1160.
12. Cahn, J.W. and Hilliard, J.E., "Free energy of a nonuniform system. I. Interfacial free energy." The Journal of chemical physics 28, no. 2 (1958): 258–267.
13. Singh, G.K., Ceder, G. and Bazant, M.Z., "Intercalation dynamics in rechargeable battery materials: general theory and phase-transformation waves in $LiFePO_4$." Electrochimica Acta 53, no. 26 (2008): 7599–7613.
14. Bai, P., Cogswell, D.A. and Bazant, M.Z., "Suppression of phase separation in $LiFePO_4$ nanoparticles during battery discharge." Nano letters 11, no. 11 (2011): 4890–4896.
15. Thorat, I.V., Joshi, T., Zaghib, K., Harb, J.N. ., "Understanding rate-limiting mechanisms in $LiFePO_4$ cathodes for Li-ion batteries." Journal of the Electrochemical Society 158, no. 11 (2011): A1185–A1193. doi:10.1149/2.001111jes
16. Farkhondeh, M. and Delacourt, C., "Mathematical modeling of commercial $LiFePO_4$ electrodes based on variable solid-state diffusivity." Journal of the Electrochemical Society 159, no. 2 (2011): A177–A192. doi:10.1149/2.073202jes
17. Safari, M. and Delacourt, C., "Mathematical modeling of lithium iron phosphate electrode: galvanostatic charge/discharge and path dependence." Journal of the Electrochemical Society 158, no. 2 (2011): A63–A73. doi:10.1149/1.3515902
18. Safari, M. and Delacourt, C., "Modeling of a commercial graphite/$LiFePO_4$ cell." Journal of the Electrochemical Society 158, no. 5 (2011): A562–A571. doi:10.1149/1.3567007
19. Dao, T.S., Vyasarayani, C.P. and McPhee, J., "Simplification and order reduction of lithium-ion battery model based on porous-electrode theory." Journal of Power Sources 198 (2012): 329–337.
20. Baba, N., Yoshida, H., Nagaoka, M., Okuda, C. ., "Numerical simulation of thermal behavior of lithium-ion secondary batteries using the enhanced single particle model." Journal of Power Sources 252 (2014): 214–228.
21. Smith, K.A., Rahn, C.D. and Wang, C.Y., "Model order reduction of 1D diffusion systems via residue grouping." Journal of Dynamic Systems, Measurement, and Control 130, no. 1 (2008): 011012.
22. Subramanian, V.R., Boovaragavan, V., Ramadesigan, V. and Arabandi, M., "Mathematical model reformulation for lithiumion battery simulations: Galvanostatic boundary conditions." Journal of the Electrochemical Society 156, no. 4 (2009): A260–A271. doi:10.1149/1.3065083
23. Cai, L. and White, R.E., "Reduction of model order based on proper orthogonal decomposition for lithium-ion battery simulations." Journal of the Electrochemical Society 156, no. 3 (2009): A154–A161. doi:10.1149/1.3049347
24. Kumar, V. S., "Reduced order model for a lithium ion cell with uniform reaction rate approximation." Journal of Power Sources 222 (2013): 426–441.
25. Ramadass, P., Haran, B., Gomadam, P.M., White, R. ., "Development of first principles capacity fade model for Li-ion cells." Journal of the Electrochemical Society 151, no. 2 (2004): A196–A203. doi:10.1149/1.1634273
26. Santhanagopalan, S., Zhang, Q., Kumaresan, K., White, R.E. , "Parameter estimation and life modeling of lithium-ion cells." *Journal of the Electrochemical Society* 155, no. 4 (2008): A345–A353. doi:10.1149/1.2839630
27. Sikha, G., Popov, B.N. and White, R.E., "Effect of porosity on the capacity fade of a lithium-ion battery theory." Journal of the Electrochemical Society 151, no. 7 (2004): A1104–A1114. doi:10.1149/1.1759972
28. Ploehn, H.J., Ramadass, P. and White, R.E., "Solvent diffusion model for aging of lithium-ion battery cells." Journal of the Electrochemical Society 151, no. 3 (2004): A456–A462. doi:10.1149/1.1644601
29. Zhang, Q. and White, R.E., "Capacity fade analysis of a lithium ion cell." Journal of Power Sources 179, no. 2 (2008): 793–798.
30. Zhang, Y., Wang, C.Y. and Tang, X., "Cycling degradation of an automotive $LiFePO_4$ lithium-ion battery." Journal of Power Sources 196, no. 3 (2011): 1513–1520.
31. Groot, J., Swierczynski, M., Stan, A.I. and Kær, S.K., "On the complex ageing characteristics of high-power $LiFePO_4$/graphite battery cells cycled with high charge and discharge currents." Journal of Power Sources 286 (2015): 475–487.
32. Verma, P., Maire, P. and Novák, P., "A review of the features and analyses of the solid electrolyte interphase in Li-ion batteries." Electrochimica Acta 55, no. 22 (2010): 6332–6341.
33. Safari, M. and Delacourt, C., "Aging of a commercial graphite/$LiFePO_4$ cell." Journal of the Electrochemical Society 158, no. 10 (2011): A1123–A1135. doi:10.1149/1.3614529
34. Vetter, J., Novák, P., Wagner, M.R., Veit, C. ., "Ageing mechanisms in lithium-ion batteries." Journal of power sources 147, no. 1 (2005): 269–281.
35. Barré, A., Deguilhem, B., Grolleau, S., Gérard, M. ., "A review on lithium-ion battery ageing mechanisms and estimations for automotive applications." Journal of Power Sources 241 (2013): 680–689.
36. Rujian, F, Song-Yul, C., Victor, A., and Jeffrey, F., "Development of a physics-based degradation model for lithium ion polymer batteries considering side reactions." Journal of Power Sources 278 (2015): 506–521.
37. Singh, G.K., Ceder, G. and Bazant, M.Z., "Intercalation dynamics in rechargeable battery materials: general theory and phase-transformation waves in $LiFePO_4$." Electrochimica Acta 53, no. 26 (2008): 7599–7613.
38. Striebel, K., Guerfi, A., Shim, J., Armand, M. ., "$LiFePO_4$/gel/natural graphite cells for the BATT program." Journal of power sources 119 (2003): 951–954.
39. Striebel, K., Shim, J., Sierra, A., Yang, H., "The development of low cost $LiFePO_4$-based high power lithium-ion batteries." Journal of Power Sources 146, no. 1 (2005): 33–38.
40. Zaghib, K., Ravet, N., Gauthier, M., Gendron, F., "Optimized electrochemical performance of $LiFePO_4$ at 60°C with purity controlled by SQUID magnetometry." Journal of power sources 163, no. 1 (2006): 560–566.
41. Dubarry, M. and Liaw, B.Y., "Identify capacity fading mechanism in a commercial $LiFePO_4$ cell." Journal of Power Sources 194, no. 1 (2009): 541–549.
42. Srinivasan, V. and Newman, J., "Existence of path-dependence in the $LiFePO_4$ electrode." Electrochemical and solid-state letters 9, no. 3 (2006): A110–A114.
43. Xueyan, L., Xiao, M., and Song-Yul, C. "Reduced order model (ROM) of a pouch type lithium polymer battery based on electrochemical thermal principles for real time applications." Electrochimica Acta 97 (2013): 66–78.

CONTACT INFORMATION

Corresponding contact

Song-Yul Choe
Mailing address: 1418 Wiggins Hall
Mechanical Engineering
Auburn University, AL, 36849
choeson@tigermail.auburn.edu
Telephone number: (+1)334-844-3328

DEFINITIONS/ABBREVIATIONS

A - sandwich area of the cell (cm^2)

a_s - specific surface area of electrode (cm^{-1})

c - ion concentration (mol L^{-1})

CHR - Cahn-Hilliard-Reaction

D - diffusion coefficient($cm^2\ s^{-1}$)

DL - deposit layer

ECM - equivalent circuit model

EIS - electrochemical impedance spectroscopy

F - Faraday constant (96,487 C mol^{-1})

FOM - full order model

I - current of the cell (A)

$\mathbf{i_0}$ - exchange current density of intercalation (Acm^{-2})

$\mathbf{j^{Li}}$ - reaction rate of intercalation (Acm^{-3})

L - thickness of the micro cell (cm)

LFP - $LiFePO_4$

OCV - open-circuit voltage (V)

PDE - partial differential equation

POD - proper orthogonal decomposition

Q - capacity of the cell (Ah)

q - concentration flux (mol cm^{-4})

R - resistance ($\Omega\ cm^2$) or universal gas constant (8.3143 J $mol^{-1}\ K^{-1}$)

$\mathbf{R_s}$ - radius of spherical electrode particle (cm)

r - coordinate along the radius of electrode particle (cm)

ROM - reduced order model

SOC - state of charge

SEI - solid electrolyte interphase

SPM - single particle model

T - cell temperature (K)

t - time (s)

 - transference number

U - potential (V)

V - voltage (V) or volume of the composite electrode (cm^3)

GREEK SYMBOLS

α - transfer coefficient for an electrode reaction

δ - thickness (cm)

ε - volume fraction of a porous medium

ϕ - electric potentials

η - overpotential (V)

κ - ionic conductivity of electrolyte (S cm^{-1})

σ - conductivity (S cm^{-1})

SUBSCRIPTS AND SUPERSCRIPTS

a - anodic

ave - average value

c - cathodic

D - diffusion

e - electrolyte phase

eff - effective

Li - Lithium ion

r - radial direction in electrode particle

s - solid phase

side - side reaction

surf - electrode particle surface

0% - 0% SOC

100% - 100% SOC

+ - positive electrode (cathode)

- - negative electrode (anode)